Understanding the spectroscopic signatures of Mn valence changes in the valence energy loss spectra of Li-Mn-Ni-O spinel oxides

M. K. Kinyanjui,[1] P. Axmann,[2] M. Mancini,[2] G. Gabrielli,[2] P. Balasubramanian,[2] F. Boucher,[3] M. Wohlfahrt-Mehrens,[2] and U. Kaiser[1]

[1]*Central Facility for Electron Microscopy, University of Ulm, Albert Einstein Allee 11, 89081 Ulm, Germany*

[2]*Centre for Solar Energy and Hydrogen Research, Helmholtzstrasse 8, 89081 Ulm, Germany*

[3]*Institut des Matériaux Jean Rouxel (IMN), Université de Nantes, CNRS, 2 rue de la Houssinière, BP 32229, 44322 Nantes cedex 3, France*

(Received 12 May 2017; revised manuscript received 13 October 2017; published 7 December 2017)

The valence energy loss spectrum which is characterized by valence-to-conduction band and plasmon excitations is rarely used in spectroscopy of Li-ion battery materials. One reason being the large number of different excitations observed in this region as well as the difficulty in interpreting their nature and origin. We have determined the nature and origin of spectral features observed in Li-Mn-Ni-O spinel oxides with respect to Mn valency changes during the insertion of lithium ion. The lithiation process is accompanied by a Mn valency change from Mn 4+ in $LiNi_{0.5}Mn_{1.5}O_4$ to Mn 3+ in lithium rich $Li_2Ni_{0.5}Mn_{1.5}O_4$. The valence energy loss spectrum of $LiNi_{0.5}Mn_{1.5}O_4$ is characterized by sharp peaks in the 7–10 eV energy loss range whose intensity decrease with lithiation to $Li_2Ni_{0.5}Mn_{1.5}O_4$. Using electronic structure calculations and molecular orbital considerations we show that the intense peaks in the valence loss spectra of $LiNi_{0.5}Mn_{1.5}O_4$ have a large contribution from ligand-metal charge transfer transitions. These transitions arise from the mainly O $2p$ nonbonding t_{2u} and bonding t_{1u} orbitals to the mainly Mn $3d$ antibonding t_{2g}^* and e_g^* orbitals. We discuss the origins of the observed valence spectra differences between the two phases in relation to peaks shift, variations in occupancy, and variations in covalency as a result of Mn valency changes occurring during lithiation.

DOI: 10.1103/PhysRevMaterials.1.074402

I. INTRODUCTION

Lithium-manganese-nickel spinel oxides (Li-Mn-Ni-O) are of interest primarily due to their applications as cathode materials in Li-ion batteries [1–5]. Some of the reasons being their relatively low costs and low toxicity especially when compared to Li-Co-O cathode materials. In addition, Li-Mn-O spinel oxides also show interesting solid state phenomena such as Jahn-Teller (JT) distortions, magnetic ordering, charge, and orbital ordering [6–9]. This class of materials, as is the case with most materials used as cathodes materials, is a transition metal oxide where one or more transition metals are bonded to oxygen. In Li-ion batteries, phase stability, voltage limits, and safety are closely related to the character of the transition metal ion in the cathode material. This includes valency, spin state, coordination, as well as interaction of the transition metal ion with the oxygen anion including hybridization, covalency, or ionicity [10–12].

Considerable research efforts have focused on understanding the evolution of transition metal valency and metal-ligand interactions such as covalency/ionicity with insertion of lithium atoms into the crystal lattice (lithiation) and extraction of lithium atoms from the crystal lattice (delithiation). Experimentally this mainly involves application of spectroscopic methods such as x-ray absorption spectroscopy (XAS) and electron energy loss spectroscopy (EELS) [13–20]. These spectroscopic methods have mainly focused on core-loss spectra originating from core states to the unoccupied states in the conduction band. Less attention has been given to valence energy loss spectra comprising valence-to-conduction band and plasmon excitations [21–24]. One reason for this has to do with the considerably large number of different types of excitations observed in this region as well as the difficulty of interpreting the origin and the nature of these excitations. These excitations include among others plasmons, which are collective excitations of valence electrons, intraband transitions, interband transitions, excitons, relativistic excitations, as well as surface and interface excitations [25,26]. Despite these difficulties, these excitations could provide a lot of information regarding the electronic structure of Li-Mn-Ni-O oxides and its evolution with lithiation/delithiation.

While signatures of Mn valence in valence EELS (VEELS) spectra of various manganese oxides have been observed, no details were given regarding the nature and the origin of these spectral features [27,28]. Here we determine the nature and the origin of the spectral signatures in the VEELS spectra that can be used to determine the effects of Mn valency changes. VEELS has several advantages compared to core-loss spectra. First, VEELS spectra are very intense with high signal to noise ratio [24]. They therefore require very much less exposure times than core-loss spectra. This leads to less beam-induced damage and could therefore be used for fast phase mapping [24]. Second, VEELS is characterized by excitations which are not observed in core-loss spectra such as plasmon excitations and intraband transitions, which are very sensitive to the doping state, as well as insulating or metallic nature of the materials under study. Third, momentum dependence of the valence excitations is sensitive to the band structure and it means momentum resolved spectroscopy of the valence-conduction band excitations can be used to study band structure [29].

II. EXPERIMENTAL AND CALCULATION DETAILS

Lithium rich $Li_2Ni_{0.5}Mn_{1.5}O_4$ phase was obtained through lithiation of $LiNi_{0.5}Mn_{1.5}O_4$ using both chemical and electrochemical lithiation methods as we described in a previous

publication [30]. EELS spectra were acquired using a Gatan-Tridiem spectrometer attached to a Titan 80–300 kV transmission electron microscope (TEM) and operating at 80 kV. At this operating voltage the energy resolution was determined to be 0.60 eV. Short exposure times in the order of 0.05–0.1 s were used during the acquisition of the VEELS spectra. To interpret and understand the nature and origins of the spectral features observed in the experiments, we calculated band structures and theoretical spectra from spinel and layered Li-Mn-O oxides with similar Mn valency. These include layered Li_2MnO_3, $LiMnO_2$, as well as cubic $LiMn_2O_4$ and tetragonal $Li_2Mn_2O_4$ spinels. Electronic structures and spectra calculations were obtained within the full potential linearized augmented plane wave (FLAPW) approximation implemented in WIEN2k code. Muffin tin radii of 1.6, 1.97, and 1.69 were used for Li, Mn, and O atoms, respectively. The parameter $Rmt * K\max$ was set to 7.5, where Rmt is the smallest atomic sphere radius in the unit cell and $K\max$ is the magnitude of the largest K vector. In order to treat the effects of local Coulomb interactions due to Mn $3d$ electrons, GGA + U method was used where the effective Coulomb parameter is being set to $U_{\text{eff}} = 4\,\text{eV}$. Antiferromagnetic (AFM) supercells were used in all cases with an AFM ordering along the b axis [31–33]. To calculate the optical properties and simulate EELS spectra, the dielectric tensor was calculated using the Optic package which is included in the WIEN2k code.

III. EXPERIMENTAL RESULTS

In Fig. 1 we compare VEELS spectra from $Li_2Ni_{0.5}Mn_{1.5}O_4$ (thin dotted curve) and $LiNi_{0.5}Mn_{1.5}O_4$ (thick solid curve). The observed spectra features are grouped into energy region (i) between 0–15 eV, (ii) between 15–30 eV, (iii) between 30–50 eV, and (iv) found above 50 eV.

To investigate the influence of Mn valency on the obtained VEELS spectra the nominal Mn valency in both and lithium rich phases was determined. Using x-ray powder diffraction supported by Rietveld refinements we previously showed that the structure of $LiNi_{0.5}Mn_{1.5}O_4$ corresponds to the ordered, cubic phase (space group $P4_332$) [30]. On the other hand, the $Li_2Ni_{0.5}Mn_{1.5}O_4$ phase is tetragonally distorted (space group $I41/amd$). The x-ray and Rietveld refinement results were supported by results obtained using selected area electron diffraction [30]. The observed cubic-to-tetragonal phase transformation with lithiation is a result of the JT distortions associated with the valency change of Mn from Mn 4+ in $LiNi_{0.5}Mn_{1.5}O_4$ to the JT active Mn 3+ ion in $Li_2Ni_{0.5}Mn_{1.5}O_4$. Similar behavior has also been shown for lithiation of the nondoped $LiMn_2O_4$ to lithium rich $Li_2Mn_2O_4$ which is also associated with a cubic-tetragonal phase transformation [34–36]

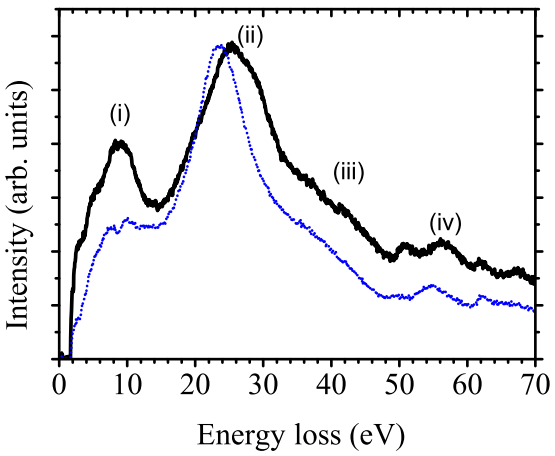

FIG. 1. Experimental valence loss electron energy loss spectra (VEELS) obtained from lithium rich $Li_2Ni_{0.5}Mn_{1.5}O_4$ (thin dotted curve) and $LiNi_{0.5}Mn_{1.5}O_4$ (thick solid curve).

IV. COMPARISON WITH CALCULATED VALENCE ENERGY LOSS SPECTRA

The effect of variations in Mn valency and related structural distortions on experimental valence energy loss experimental spectra was explored using electronic/band-structure calculations and the calculated VEELS spectra. Theoretical spectra and electronic structures from *ab initio* calculations have already been shown to be useful in interpreting experimental EELS spectra and vice versa [21–23]. Figure 2(a) displays the calculated energy loss functions (ELF) for cubic spinel $LiMn_2O_4$ (Mn 3.5+, thick solid curve), and $Li_2Mn_2O_4$ (Mn 3+, thin dotted curve). In Fig. 2(b) we display calculated ELF for $LiMnO_2$ (Mn 3+, thin dotted curve) and Li_2MnO_3 (Mn 4+, thick solid curve), respectively. Comparing calculated ELF with the experimental VEELS spectra in Fig. 1, we observe that the features in the ELF for Li-Mn-O oxides with higher Mn valency ($LiMn_2O_4$ and Li_2MnO_3) match the experimental spectra from $LiNi_{0.5}Mn_{1.5}O_4$. Similarly, the spectra from Li-Mn-O oxides with valency Mn 3+ ($Li_2Mn_2O_4$ and $LiMnO_2$) match the spectra from $Li_2Ni_{0.5}Mn_{1.5}O_4$. This is especially the case for the intensity of the peak (i) found

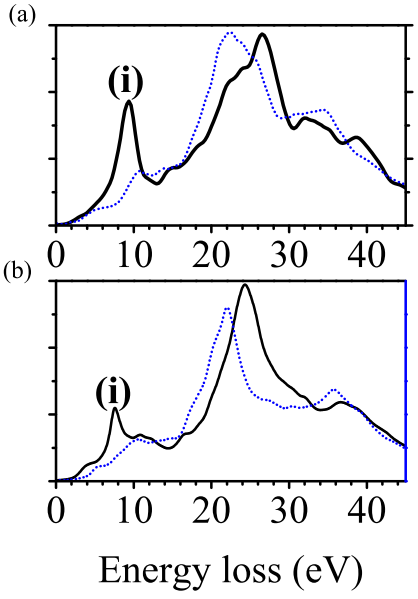

FIG. 2. (a) Calculated energy loss functions (ELF) for cubic spinel $LiMn_2O_4$ (Mn 3.5+, thick solid curve) and $Li_2Mn_2O_4$ (Mn 3+, thin dotted curve). (b) Layered Li_2MnO_3 (Mn 4+, thick solid curve) and $LiMnO_2$ (Mn3+, thin dotted curve).

around 7–10 eV in all phases. This peak is much more intense in Li-Mn-O oxide with a higher Mn valency

V. NATURE AND ORIGIN OF THE OBSERVED SPECTRA FEATURES

A. Comparison with band structure calculations

VEELS spectra probe the joint density of states (JDOS) where JDOS is a convolution of valence and conduction density of states [25,26]. Density of states (DOS) calculations are therefore an important step towards understanding spectra features in valence energy loss spectra [21–23]. From calculated ELF presented in Fig. 2 we observe that the VEELS spectra for both spinel and layered Li-Mn-O oxides shows similar features with the only difference being variations in intensity of peak (i) related to the change in Mn valency. In the following discussion we will use electronic structure and spectra calculations of Li_2MnO_3 as a standard to understand the electronic structure of Li-Mn-O structures and the influence of Mn valency on the valence energy loss spectra. The symmetry projected partial density of states (PDOS) from Mn $3d$, Mn $4s/4p$, O $2s$, and O $2p$ from Li_2MnO_3 are shown in Figs. 3(a)–3(d), respectively.

From the PDOS we observe that the energy states at the Fermi level are dominated by Mn $3d$ and O $2p$ states [31,34]. The corresponding band structure for Li_2MnO_3 is shown in Fig. 4 for majority (solid thin line) and minority spins (dashed thin line). In the band structure, bands 50, 65, and 75 below the Fermi level and bands 80, 85, 90, and 100 above the Fermi level are indicated (thick dashed line).

The radius of the circles represents the Mn $3d$ character of each band. The bands characterized by larger circles correspond to bands with more Mn $3d$ character. The bands with smaller circles correspond to bands with less Mn $3d$ character. The larger the circle the more $3d$ character a band shows. Based on the PDOS results presented in Fig. 3 and the band structure, it can be seen that the energy region encompassing bands 50, 65, 75, 80, 85, and 90 is of mainly Mn $3d$ and O $2p$ character. On the other hand, band 100 is

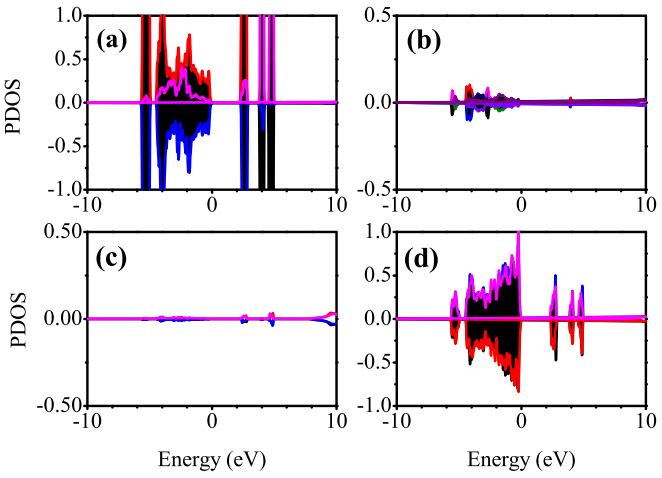

FIG. 3. Symmetry projected partial density of states (PDOS) for (a) Mn $3d$, (b) Mn $4s/4p$, (c) O $2s$, and (d) O $2p$ for the Li_2MnO_3 phase.

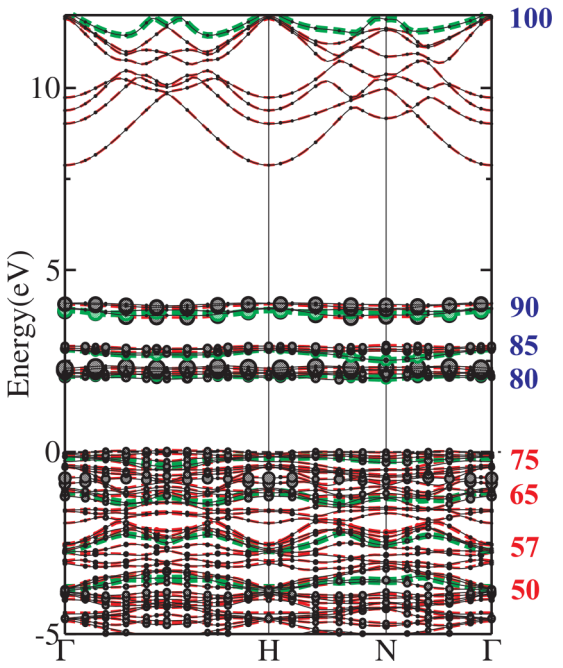

FIG. 4. Li_2MnO_3 band structure for majority spin (solid thin line) and minority spin (dashed thin line). Bands 50, 57, 65, and 75 below the Fermi level and bands 80, 85, and 90 above the Fermi level are also indicated (thick dashed line) The radius of the circles represents the Mn $3d$ character of each band with a large circle showing more Mn $3d$ character and vice versa.

found in the energy region with mainly Mn $4s/4p$ character. In particular, we observe that the bands at the top of the valence band including band 75 are mainly of Mn $3d$ character. On the other hand, the group of bands between bands 65 and 50 has less Mn $3d$ character as shown by the small radius of the circles. These bands show more O $2p$ character. Below band 50 is another group of bands with more Mn $3d$ character.

Through electronic and theoretical spectra calculations it is possible to determine the origin and the nature of interband transitions which contribute to the valence energy loss spectra [21–23,29]. The calculated ELF can be expressed as $\mathrm{ELF} = \mathrm{Im}(-\varepsilon^{-1}) = \varepsilon_2/(\varepsilon_1{}^2 + \varepsilon_2{}^2)$, where ε, ε_1, and ε_2 are the dielectric function, real, and imaginary parts of the dielectric function, respectively [25,26]. Valence-to-conduction band interband transitions contribute to the peaks observed in the imaginary part of the dielectric function ε_2. Furthermore, partial ε_2 functions can be calculated by decomposing the calculated ε_2 function into a pair or a group of valence and conduction bands contributing to peaks in the ε_2 curve [21,23,24]. Subsequently, partial ELF can then be calculated to show the contribution of various interband transitions on the peaks in the energy loss function (ELF) [23]. Therefore, in the case where the theoretical spectra match experimental spectra, one can assign peak features in an experimental spectra to specific interband transitions as well as determine their character

In Figs. 5(a)–5(c) we display calculated partial ELF for Li_2MnO_3 involving transitions from a group of occupied bands between 50–78, 65–78, and 75–78 below the Fermi level to a group of unoccupied bands 79–80, 79–85, 79–90, and

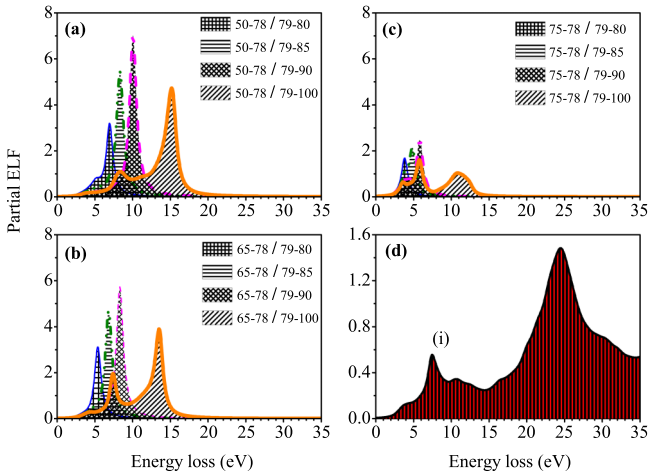

FIG. 5. Calculated partial energy loss functions (ELF) for transitions between group of occupied bands (a) 50−78, (b) 65−78, and (c) 75−78 to the group of unoccupied bands 79−80, 79−85, 79−90, and 79−100 above the Fermi level, respectively. Bands 78 and 79 are the highest occupied and lowest empty band, respectively, and (d) full ELF for Li_2MnO_3.

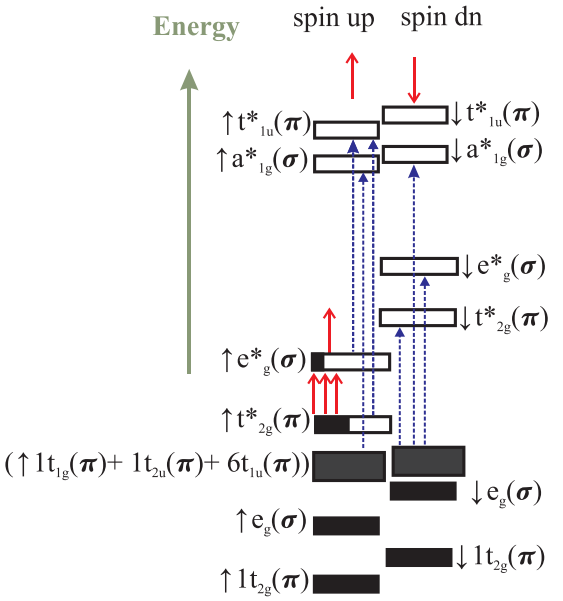

FIG. 6. A schematic molecular orbital diagram from a MnO_6^{9-} cluster with Mn 3+ after Ref. [37]. The dark squares represent filled states and the unfilled rectangles show the unfilled states. The solid arrows show the occupying spin of the electron, while dashed arrows show the possible interband transitions.

79–100 above the Fermi level. Bands 78 and 79 are the highest occupied and lowest empty band, respectively. Figure 5(d) displays the full ELF for Li_2MnO_3 showing the position of peak (i) whose intensity was shown to be to be sensitive to Mn valency in the experiments and calculations.

The lowest interband transitions consist of transitions from bands 75 to bands 80, 85, and 90 with mainly 3*d* character located at/near the Fermi level. These transitions make contributions to ELF peaks found at energy up to 5 eV. Transitions from bands 75–78 to band 100 also make a contribution to the peaks above 10 eV. From the partial ELF shown we see the interband transitions from bands 50–65 to bands 85–90 above the Fermi level make the largest contribution to the intensity of peak (i) at energy region 7–10 eV. From the band structure plot we also observe that bands 50–65 have less Mn 3*d* character as compared to band 75 for example, since the radius of the circles representing the Mn 3*d* character is smaller in band 65 than band 75. On the other hand, bands 85–90 are bands with mainly metal 3*d* character. Therefore the interband transitions from bands 50–65 and which contribute to the intensity of peak (i) are of ligand-metal charge transfer type since they originate from states with mainly ligand character to a state with mainly metallic character.

B. Comparison with molecular orbital model

The band structure analysis presented in the previous section can be compared to the molecular orbital approach (MO) previously used to understand bonding and spectroscopy in various transition metal oxides [37–46]. In the MO approach the electronic structure and bonding of transition metal oxides is approximated by bonding interactions involving a central metal ion (Me) co-coordinated to six oxygen (O) ligands within a MeO_6 octahedra [40]. In Fig. 6 we show a schematic of the molecular orbital (MO) diagram for a MnO_6^{9-} cluster with Mn valency of Mn 3+ after Sherman *et al.* [37]. The diagram shows hybridized molecular orbitals which are formed from Mn and O atomic orbitals. Oxygen ligand orbitals include the O 2*s* and O 2*p* ($2px$, $2py$, $2pz$) orbitals which are hybridized as $\sigma(2s\text{-}2pz)$ and $\pi(2px, 2py)$. The metal orbitals involved include Mn 3*d*, 4*s*, and 4*p*. Hybridization of $\sigma(2s\text{-}pz)$ with Mn 3*d*, 4*s*, and 4*p* orbitals result in σ molecular orbitals. These include bonding e_g, a_{1g}, and t_{1u} and the respective antibonding e_g^*, a_{1g}^*, and t_{1u}^* molecular orbitals. Hybridization of π(2px, $2py$) with Mn 3*d* and Mn 4*p* results in π molecular orbitals specifically bonding t_{2g}, t_{1u} and antibonding t_{2g}^*, t_{1u}^* molecular orbitals. The nonbonding orbitals from $\pi(2px, 2py)$ orbitals include the t_{1g} and t_{2u} molecular orbitals [38,40].

In Fig. 6 all ligand bonding and nonbonding orbitals are filled. The dark squares display the filled states while the unfilled rectangles represent the unfilled states. The solid arrows show the occupying spin of the electron while the dashed arrows show possible interband transitions. The general structure of hybridized molecular orbitals obtained in the MO approach agrees quite well with the band structure calculations. From the MO diagram we see that highest occupied and lowest unoccupied orbitals are the antibonding $e_g^*(\sigma)$ and $t_{2g}^*(\pi)$ which are partially filled giving $(\uparrow\ t_{2g}^{*3})(\uparrow\ e_g^{*1})$ for Mn 3+ and $(\uparrow t_{2g}^{*3})$ for Mn 4+. This corresponds to the band structure region encompassing bands 75, 80, 85, and 90 shown in Fig. 4. The mainly ligand t_{1g}, t_{2u}, and t_{1u} orbitals are found below the e_g^* and t_{2g}^* orbitals. Comparing this with the band structure in Fig. 4, we observe that bands 50–65 are found in the band structure region which corresponds to the mainly ligand t_{1g}, t_{2u}, and t_{1u} orbitals.

The added importance of the MO diagram in the current discussion is that it allows for the determination of allowed interband transitions as dictated by spin and sym-

metry selection rules [37,45]. Transitions between orbitals of the same symmetry (g → g and $u \rightarrow u$) are forbidden while transitions involving orbitals of different symmetry ($g \rightarrow u$ and $u \rightarrow g$) are allowed. Spin selection rules also dictate that allowed transitions should not change the electron spin state [37,41]. Some of the allowed transitions include (1) $[a_{1g}(\sigma), e_g(\sigma), a_{1g}(\sigma), t_{2g}(\pi), t_{1g}(\pi)] \rightarrow t^*_{1u}(\sigma)$, (2) $[t_{1u}(\sigma), t_{1u}(\pi)] \rightarrow a^*_{1g}(\sigma)$, (3) $[t^*_{2g}(\pi), e^*_g(\sigma)] \rightarrow [t^*_{1u}(\sigma)]$, (4) $[t_{1u}(\sigma), t_{1u}(\sigma)] \rightarrow (t^*_{2g}, e^*_g)$, and (5) $[t_{1u}(\pi), t_{2u}(\pi)] \rightarrow [t^*_{2g}(\pi), e^*_g(\sigma)]$ [37]. As can be deduced from Fig. 6, most of the spin and allowed transitions are ligand-to-metal and metal-ligand-charge transfer transitions. Ligand-to-metal charge transfer transitions include transitions from mainly ligand orbitals (t_{1u} and t_{2u}) to mainly antibonding metallic orbitals (t^*_{2g} and e^*_g). Metal-to-ligand charge transfer are at a much higher energy and include transitions from mainly antibonding metallic orbitals (t^*_{2g} and e^*_g) to mainly ligand antibonding orbitals.

There are two important characteristics of the MO diagrams important for the current discussion. The first is the exchange interaction which results in the splitting of orbitals into majority spin (spin-up) and minority spin (spin-down) where the exchange energy splitting is the energy between the spin-up ($\uparrow t^*_{2g}$) and spin-down states ($\downarrow t^*_{2g}$) [37,45]. Second is the crystal field splitting which is the energy separating the crystal field orbitals ($\uparrow t^*_{2g}$) and ($\uparrow e^*_g$). Sherman *et al.* have shown that the empty ($\downarrow t^*_{2g}$), ($\downarrow e^*_g$) states are at higher energy for MnO_6^{9-} cluster with Mn^{3+} when compared to MnO_6^{8-} cluster with Mn 4+ [37]. The position of nonbonding ligand orbitals (t_{1g} and t_{2u}) on the other hand does not change much with Mn valency changes [37]. Based on both band structure and MO analysis it becomes clear that peak (i) in the valence spectra of $LiNi_{0.5}Mn_{1.5}O_4$ has a large contribution from ligand-metal charge transfer transitions involving the bonding and nonbonding O 2p states of t_{2u} and t_{1u} symmetry to the metallic 3d states e^*_g, t^*_{2g}.

VI. ORIGIN AND NATURE OF OBSERVED SPECTRA DIFFERENCES

Due to strong O 2p/Mn 3d hybridization, changes in the valency of the Mn ions will also affect the O 2p states through changes in the degree of hybridization, the position of the various orbitals, exchange, and ligand field splitting. This then results in the changes observed in VEELS spectra. These changes can be grouped into two categories. (1) Changes involving peak positions and (2) changes involving peak intensity. In the following discussion we examine how these peak characteristics are related to Mn valency changes with lithiation of $LiNi_{0.5}Mn_{1.5}O_4$ to $Li_2Ni_{0.5}Mn_{1.5}O_4$

A. Peak position

In both core and valence electron energy loss spectra, positions of the peaks rising from single electron transitions are related to the energy difference between the initial state and the final state of a specific transition. The intense peak (i) observed in the valence spectra of $LiNi_{0.5}Mn_{1.5}O_4$ (see Fig. 1) was determined to have a large contribution from ligand-to-metal charge transfer transitions arising largely from the nonbonding state t_{2u} and bonding t_{1u} states having mainly O 2p character to antibonding metal e^*_g and t^*_{2g} states having mainly Mn 3d character. Changes in Mn valency result in the shift of the energy positions of orbitals showing Mn character. The position of nonbonding O 2p orbitals on the other hand does not change with changes in the Mn valency. Several variations in orbital positions are observed with respect to changes in the Mn valence. The first observation is that the entire d band shifts in energy with changes with valency [47]. An increase in the oxidation state for example Mn 3+ to Mn 4+ results in a decrease in the energy of d orbitals. The second observation is that changes in the Mn valency affects the crystal field energy between ($\uparrow e^*_g$) and ($\downarrow t^*_{2g}$) [37,45]. The third effect is on the exchange spin energy which is the energy between the majority spin ($\uparrow t^*_{2g}$) and minority spin ($\downarrow t^*_{2g}$) [37]. Increasing the oxidation state of Mn results in the increase in the ligand field splitting and decrease in the exchange splitting which is the energy separating spin-up and spin-down states. In $LiNi_{0.5}Mn_{1.5}O_4$ (Mn 4+) the energy gap between the nonbonding O 2p states of t_{2u} and t_{1u} to the metallic antibonding states e^*_g, t^*_{2g} is lower than in $Li_2Ni_{0.5}Mn_{1.5}O_4$ (Mn 3+). This means that peaks which arises from (t_{2u}, t_{1u}) → (e^*_g, t^*_{2g}) transitions are shifted to higher energy position in $Li_2Ni_{0.5}Mn_{1.5}O_4$ when compared to $LiNi_{0.5}Mn_{1.5}O_4$.

B. Peak intensity

Several factors may influence peak intensity differences observed in the experimental VEELS spectra. These include variations in transition probability, covalency, shifts in peak positions, as well as structural transformation and anisotropy associated with changes in Mn valency. Generally, in EELS the intensity of single electron transitions can be approximated as $I \sim M(E)2N(E) \sim df/dE\, N(E)$ after correcting for background and multiple scattering $M(E)$ are the matrix elements related to oscillator strength df/dE and $N(E)$ is the density of final states [26]. The probability of a transition is therefore proportional to the density of the unoccupied final states and matrix element representing the degree of overlap between the initial and the final state [26]. In valence energy loss spectra, single electron transitions (interband transitions) make contributions to the peaks in the imaginary part of the dielectric function (ε_2). The intensity of these peaks is proportional to the oscillator strength and the joint density of states (JDOS) [25,26]. Within the dipole approximation, the probability of a transition is therefore higher if the density of unoccupied final states being probed by the transition is large. This is then reflected in a higher intensity of the allowed transition. In the case of pristine and lithium rich phases investigated in this paper, more unoccupied Mn 3d states are available for transitions in $LiNi_{0.5}Mn_{1.5}O_4$ (Mn 4+, t^{*3}_{2g}) than in $L_2Ni_{0.5}Mn_{1.5}O_4$ (t^{*3}_{2g}, e^{*1}_g). The probability of transitions is therefore higher in $LiNi_{0.5}Mn_{1.5}O_4$ (t^{*3}_{2g}) than in $Li_2Ni_{0.5}Mn_{1.5}O_4$ (t^{*3}_{2g}, e^{*1}_g). Subsequently the peaks due to ligand-metal charge transfer are more intense in $LiNi_{0.5}Mn_{1.5}O_4$ (t^{*3}_{2g}). Indeed experiments and calculations based on the related Cr oxides and halides show that ligand-to-metal charge transfer excitations are favored when the metal ion is in a higher oxidation state [48–50].

The effects of covalency on peak intensity have been investigated in several transition metal oxides and halides using core-loss spectroscopy. The effects of covalency are especially apparent in the intensity variations at the pre-edge peak of the ligand K edge [43,47,51,53]. The intensity of the pre-edge peaks at the ligand K edge has been shown to be very sensitive to the degree of hybridization between the transition metal d states and ligand p states [43,53]. The intensity of the pre-edge peaks therefore increases with increased covalency between the transition metal $3d$ and the halide and oxygen ligand p states. In particular, an increase in intensity of the pre-edge peak with increased covalency is also related to the increase in the oxidation state of the metal ion [43,53]. This is attributed to the effective nuclear charge of the ion [47]. The effective nuclear charge (Z_{eff}) of the transition metals increases with increasing oxidation, for example, $Z_{\text{eff}}\,\text{Mn}4+ > Z_{\text{eff}}\,\text{Mn}3+$ [47]. An increased effective nuclear charged on the metal means that the d orbitals are at deeper binding energy increasing the interaction between the metal $3d$ orbitals and the lower lying O $2p$ states. This leads to increased hybridization/covalency with higher oxidation state of the Mn ion.

Similarly, variation in the degree covalency with Mn valency can affect the intensity of peaks arising from interband transition in valence energy loss spectra. A reason for this is that the intensity associated with charge transfer interband transitions excitation from filled ligand orbitals to partially occupied metallic antibonding t_{2g}^* and e_g^* orbitals also reflects the character of the metal-ligand bonding [48–53]. The intensity of the charge transfer transitions is given as being proportional to (RS) [2] where S is the overlap of the donor and acceptor orbitals and the R is the metal-ligand bond length [52,53]. The intensity of charge transfer transitions is therefore higher with increasing overlap between the metal and the ligands. The degree of ligand-metal overlap/covalency increases with increasing oxidation state of the metal ion. This means that an increase in the oxidation state of the metal ion will be reflected by an increase in the intensity of peaks related to charge transfer interband transitions. In the present case $LiNi_{0.5}Mn_{1.5}O_4$ with Mn 4+ is more covalent than $Li_2Ni_{0.5}Mn_{1.5}O_4$ with Mn 3+. The high intensity of the peaks due to ligand-metal charge transfer transitions in the valence loss spectra of $LiNi_{0.5}Mn_{1.5}O_4$ therefore reflects the increased covalency of the Mn-O bond with increased oxidation state

Shifts in the peak energy positions associated with Mn valence change may also lead to change in the intensity of the peaks observed in the EELS spectra. In VEELS spectra a shift in the peak position to higher energies may also lead to peak features being covered by the broad intensity background due to volume plasmon excitation. This leads to the reduction of the observed peak intensity. The fourth factor that may influence the intensity of the observed peaks is the structural anisotropy due to structural transformation related to the JT distortions. Due to JT distortions associated with Mn valency changes, the crystal structure changes from cubic in $LiNi_{0.5}Mn_{1.5}O_4$ to tetragonal in $Li_2Ni_{0.5}Mn_{1.5}O_4$. The resulting structural anisotropy means that the intensity of the peaks associated with charge transfer transitions may vary depending on the crystal direction. An additional effect of the Jahn-teller distortion in Mn 3+ is to split the states with e_g^* antibonding orbital into b_{1g} symmetry (d_{x2-y2}) and a_{1g} symmetry (d_{z2}), while t_{2g} states are split into b_{2g} symmetry (d_{xy}) and e_g symmetry (d_{xz}, d_{yz}) [11]. If the energy gap between these Jahn-teller distorted states is smaller than the resolution of the spectra it results in broadening of the peaks and reduction of intensity.

VII. CONCLUSIONS

In this paper we have investigated the nature and origin of the spectral features observed in the valence energy loss spectra with respect to Mn valency changes during the lithiation of $LiNi_{0.5}Mn_{1.5}O_4$ to lithium rich $Li_2Ni_{0.5}Mn_{1.5}O_4$. The lithiation process is characterized by a cubic-tetragonal structural transformation and Mn valency change from Mn 4+ in cubic $LiNi_{0.5}Mn_{1.5}O_4$ to Mn 3+ in lithium rich tetragonal $Li_2Ni_{0.5}Mn_{1.5}O_4$. The valence energy loss spectra of $LiNi_{0.5}Mn_{1.5}O_4$ is characterized by intense peaks in the energy region 7–10 eV. The intensity of these peaks is reduced in $Li_2Ni_{0.5}Mn_{1.5}O_4$ band structure calculations and molecular orbital considerations show that the intense peaks in the valence loss spectra of $LiNi_{0.5}Mn_{1.5}O_4$ have a significant contribution from ligand-metal charge transfer transitions from the mainly ligand O $2p$ nonbonding t_{2u} and bonding t_{1u} orbitals to the mainly metallic Mn $3d$ antibonding t_{2g}^* and e_g^* orbitals. The origins of the observed spectral intensity difference between the two phases are due to shifts in peaks positions, structural anisotropy, and variations in transition probability due to changes in $3d$ occupancy, and covalency as result of changes in Mn valency.

[1] J. M. Tarascon, E. Wang, F. K. Shokoohi, W. R. McKinnon, and S. Colson, J. Electrochem. Soc. **138**, 2859 (1991).
[2] Q. Zhong, A. Bonakdarpour, M. Zhang, Y. Gao, and J. R. Dahn, J. Electrochem. Soc. **144**, 205 (1997).
[3] K. Amine, H. Tukamoto, H. Yasuda, and Y. Fujita, J. Electrochem. Soc. **143**, 1607 (1996).
[4] M. Wohlfahrt-Mehrens, A. Butz, and R. Oesten, J. Power Sources **68**, 582 (1997).
[5] J.-H. Kim, S.-T. Myung, C. S. Yoon, S. G. Kang, and Y.-K. Sun, Chem. Mater. **16**, 906 (2004).
[6] A. S. Wills, N. P. Raju, and J. E. Greedan, Chem. Mater. **11**, 1510 (1999).
[7] J. Rodriguez-Carvajal, G. Rousse, C. Masquelier, and M. Hervieu, Phys. Rev. Lett. **81**, 4660 (1998).
[8] A. Van der Ven, C. Marianetti, D. Morgan, and G. Ceder, Solid State Ionics **135**, 21 (2000).
[9] J. Goodenough, Annu. Rev. Mater. Sci. **28**, 1 (1998).
[10] J. Reed and G. Ceder, Chem. Rev. **104**, 4513 (2004).
[11] J. B. Goodenough and Y. Kim, J. Solid State Chem. **182**, 2904 (2009).

[12] C. M. Julien, A. Mauger, K. Zaghib, and H. Groult, Inorganics **2**, 132 (2014).
[13] J. R. Croy, M. Balasubramanian, D. Kim, S. H. Kang, and M. Thackeray, Chem. Mater. **23**, 5415 (2011).
[14] W. S. Yoon, K. Y. Chung, K. H. Oh, and K. B. Kim, J. Power Sources **119–121**, 706 (2003).
[15] F. Cosandey, *Microscopy: Science, Technology, Applications and Education*, (FORMATEX, Badajoz, 2010), Vol. 3, p. 1662.
[16] A. K. Shukla, Q. M. Ramasse, C. Ophus, H. Duncan, F. Hage, and G. Chen, Nat. Commun. **6**, 8711 (2015).
[17] Y. Koyama, T. Mizoguchi, H. Ikeno, and I. Tanaka, J. Phys. Chem. B **109**, 10749 (2005).
[18] S. Miao, M. Kocher, P. Rez, B. Fultz, R. Yazami, and C. C. Ahn, J. Phys. Chem. A **111**, 4242 (2007).
[19] D. Ensling, G. Cherkashinin, S. Schmid, S. Bhuvaneswari, A.Thissen, and W. Jaegermann, Chem. Mater. **26**, 3948 (2014).
[20] J. Graetz, A. Hightower, C. C. Ahn, R. Yazami, P. Rez, and B Fultz, J. Phys. Chem. B **106**, 1286 (2002).
[21] F. Espinosa-Magana, L. Alvarez-Contreras, O. Morales-Rivera, M. T. Ochoa-Lara, S. M. Loya-Mancilla, and A. Aguilar-Elguezabal, J. Phys. Chem. Solids **70**, 972 (2009).
[22] V. Mauchamp, F. Boucher, and P. Moreau, Ionics **14**, 191 (2008).
[23] M. K. Kinyanjui, P. Axmann, M. Wohlfahrt-Mehrens, P. Moreau, F. Boucher, and U. Kaiser, J. Phys.: Condens. Matter **22**, 275501 (2010).
[24] P. Moreau, V. Mauchamp, F. Pailloux, and F. Boucher, Appl. Phys. Lett. **94**, 123111 (2009).
[25] J. Fink, Adv. Electron El. Phys. **75**, 121 (1989).
[26] R.F. Egerton, Rep. Progr. Phys. **72**, 016502 (2009).
[27] J. H. Paterson and O. L. Krivanek, Ultramicroscopy **32**, 319 (1990).
[28] J. H. Rask, B. A. Miner, and P. R. Buseck, Ultramicroscopy **21**, 321 (1987).
[29] M. K. Kinyanjui, G. Benner, G. Pavia, F. Boucher, H.-U. Habermeier, B. Keimer, and U. Kaiser, Appl. Phys. Lett. **106**, 203102 (2015).
[30] M. Mancini, P. Axmann, G. Gabrielli, M. Kinyanjui, U. Kaiser, and M. Wohlfahrt-Mehrens, ChemSusChem **9**, 1843 (2016).
[31] C. Y. Ouyang, S. Q. Shi, and M. S. Lei, J. Alloys Compd. **474**, 370 (2009).
[32] G. Singh, S. L. Gupta, R. Prasad, S. Auluck, R. Gupta, and A. Sil, J. Phys. Chem. Solids **70**, 1200 (2008).
[33] H. Berg, K. Göransson, B. Noläng, and J. O. Thomas, J. Mater. Chem. **9**, 2813 (1999).
[34] Y. Liu, T. Fujiwara, H. Yukawa, and M. Morinaga, Electrochim. Acta **46**, 1151 (2001).
[35] T. Ohzuku, M. Kitagawa, and T. Hirai, J. Electrochem. Soc. **137**, 769 (1990).
[36] M. M. Thackeray, W. I. F. David, P. G. Bruce, and J. B. Goodenough, Mater. Res. Bull. **18**, 461 (1983).
[37] D. M. Sherman, Am. Mineral. **69**, 788 (1984).
[38] D. W. Fischer, Phys. Rev. B **5**, 4219 (1972).
[39] J. A. Tossell, J. Electron Spectrosc. Relat. Phenom. **8**, 1 (1976).
[40] C. J. Ballhausen and H. B. Gray, *Molecular Orbital Theory* (Benjamin, New York, 1965).
[41] A. S. Moskvin, A. A. Makhnev, L. V. Nomerovannaya, N. N. Loshkareva, and A. M. Balbashov, Phys. Rev. B **82**, 035106 (2010).
[42] H. Kurata and C. Colliex, Phys. Rev. B **48**, 2102 (1993).
[43] R. Qiao, T. Chin, S. J. Harris, S. Yan, and W. Yang, Curr. Appl. Phys. **13**, 544 (2013).
[44] L. A. Grunes, R. D. Leapman, C. N. Wilker, R. Hoffmann, and A. B. Kunz, Phys. Rev. B **25**, 7157 (1982).
[45] D. W. Fischer, J. Phys. Chem. Solids **32**, 2455 (1971).
[46] H. H. Tippins, Phys. Rev. B **1**, 126 (1970).
[47] S. E. Shadle, B. Hedman, K. O. Hodgson, and E. I. Solomon, J. Am. Chem. Soc. **117**, 2259 (1995).
[48] A. van der Avoird and P. Ros, Theoret. Chim. Acta. (Berlin) **4**, 13 (1966).
[49] J. F. Dillon, H. Kamimura, and J. P. Remeika, J. Phys. Chem. Solids **27**, 1531 (1966).
[50] Y. Sakisaka, H. Kato, and M. Onchi, Surf. Sci. **120**, 150 (1982).
[51] F. Neese, B. Hedman, K. O. Hodgson, and E. I. Solomon, Inorg. Chem. **38**, 4854 (1999).
[52] T. Glaser, B. Hedman, K. O. Hodgson, and E. I. Solomon, Acc. Chem. Res. **33**, 859 (2000).
[53] E. I. Solomon, D. W. Randall, and T. Glaser, Coord. Chem. Rev. **200–202**, 595 (2000).